

# Chemical evolution of an isolated power plant plume during the TexAQS 2000 study<sup>☆</sup>

Stephen R. Springston\*, Lawrence I. Kleinman, Frederick Brechtel<sup>1</sup>,  
Yin-Nan Lee, Linda J. Nunnermacker, Jian Wang

*Brookhaven National Laboratory, Upton, NY 11973, USA*

Received 2 November 2004; received in revised form 20 January 2005; accepted 20 January 2005

## Abstract

Stack emissions from a coal-burning power plant were measured during a research flight of the DOE G-1 during the Texas Air Quality Study (TexAQS 2000) on 10 September 2000. Clean upstream air and an isolated location allowed the plume to be unambiguously sampled during 12 successive downwind transects to a distance of 63 km—corresponding to a processing time of 4.6 h. The chemical transformation rates of sulfur and nitrogen primary pollutants into aerosol  $\text{SO}_4^{2-}$  and  $\text{HNO}_3$  yield independent values of OH concentration ( $8.0$  and  $11 \times 10^6 \text{ cm}^{-3}$ , respectively) that are consistent within experimental uncertainty and qualitatively agree with constrained steady-state (CSS) box model calculations. Ozone production efficiency increases with plume age as expected. Primary aerosol emissions with  $D_p > 5 \mu\text{m}$  were sampled near the stack. As the plume ages, aerosol size distributions adjusted for dilution show constant number concentrations of aerosols  $D_p > 10 \text{ nm}$  and a marked increase in accumulation-mode particles ( $D_p > 0.1 \mu\text{m}$ ) as gas-to-particle-conversion causes smaller particles to grow.

© 2005 Elsevier Ltd. All rights reserved.

**Keywords:** Power-plant plume; Texas 2000 Air Quality Study; Aerosol growth; Airborne measurements

## 1. Introduction

Power plants are responsible for 72 and 25% of the  $\text{SO}_2$  and  $\text{NO}_x$  emissions in the US (EPA, 2004). Over much of the US,  $\text{SO}_4^{2-}$  constitutes 50% or more of  $\text{PM}_{2.5}$ , making

power plants the single largest contributor to the fine particle aerosol loading (Malm et al., 2004). A single power plant can emit more  $\text{NO}_x$  than a mid-sized city leading to high  $\text{O}_3$  concentrations downwind. There have been many studies in power plant plumes yielding data on the formation rate of aerosol  $\text{SO}_4^{2-}$ , the oxidation rate of  $\text{NO}_x$ , and the efficiency of  $\text{O}_3$  production, defined as the number of molecules of  $\text{O}_3$  formed per  $\text{NO}_x$  molecule oxidized (Gillani et al., 1998; Nunnermacker et al., 2000; Hewitt, 2001; Ryerson et al., 2001). Other studies have focused on the size distributions of aerosols formed in plumes (McMurry et al., 1981; Brock et al., 2002). In only a few cases have aerosol particle size distributions, gas–gas and gas–particle conversion rates and  $\text{O}_3$  production efficiency (OPE) been simultaneously determined.

<sup>☆</sup> By acceptance of this article, the publisher and/or recipient acknowledges the US Government's right to retain a non-exclusive, royalty-free copyright covering this paper. This research was performed under the auspices of the United States Department of Energy under Contract No. DE-AC02-98CH10886.

\*Corresponding author.

<sup>1</sup> Now at Brechtel Mfg. Inc., 1789 Addison Way, Hayward, CA 94544, USA.

Most daytime power plant kinetic studies in cloud-free conditions show that aerosol  $\text{SO}_4^{2-}$  is formed from the oxidation of  $\text{SO}_2$  by OH radical. Daytime  $\text{NO}_x$  oxidation is also consistent with OH chemistry, but the two measures often give different OH concentration estimates. Ozone production efficiencies have been measured in plumes with low and high  $\text{NO}_x$  emissions and under conditions where background air has low and high VOC reactivity. OPE is observed to decrease with increasing  $\text{NO}_x$  emissions and is higher in regions with biogenic isoprene emissions (Lunia et al., 2000; Ryerson et al., 2001). Evolution of aerosol size distributions in power plant plumes under cloud-free conditions is generally consistent with the accumulation of aerosol mass by a condensation process.

We report here aircraft measurements made in the Sandow power plant plume conducted as part of the TexAQs 2000 field campaign. This plant, located in rural Milam County, Texas 180 km NW of Houston, generates a total of 900 MW from four boilers burning  $5.6 \text{ Mton yr}^{-1}$  of locally produced lignite to supply electricity for a collocated aluminum smelter and the commercial power grid. The site's tallest stack is 161 m high. Stated emissions from the plant are given in Table 1. The terrain rises gradually from 141 m at the site to 160 m near the north western end of the flight track. (Elevations and aircraft altitudes are given as above mean sea level.) Vegetation was comprised of grasses and scattered trees. No significant highways or population centers impact the sampled region or the area immediately upwind.

There are several features of the Sandow plant that make it an interesting candidate to study. Sandow is remotely located, so its stack plume can be unambiguously identified and studied without interferences from other emission sources. Sandow is the largest lignite fueled power plant in the US. Compared to other fuels, lignite has a low energy content and produces fly ash that is hard to capture with an electrostatic precipitator. Combustion characteristics of lignite are different from that of other fuels as evidenced by Sandow's high CO emission rate,  $21 \text{ kton yr}^{-1}$ .  $\text{SO}_2$  emissions are high ( $80 \text{ kton yr}^{-1}$ ) as 3 of the 4 units at Sandow were built in the early 1950s and were not required to meet the new

standards put into place in the 1970s. The 3 grandfathered units at Sandow are not equipped with flue gas desulfurization scrubbers and are only required to meet more lenient standards based on the sulfur content of the locally available lignite. However, these standards are slated to change.

Using data from the DOE G-1 aircraft, the conversion rate of  $\text{SO}_2$  to aerosol sulfate was estimated by measuring an increase in aerosol volume with processing time. Changes in the  $\text{NO}_x$  to  $\text{NO}_y$  ratio were similarly used to determine the rate of  $\text{NO}_x$  oxidation. Correlations between  $\text{O}_x$  ( $\text{O}_3 + \text{NO}_2$ ) and  $\text{NO}_x$  oxidation products ( $\text{NO}_z = \text{NO}_y - \text{NO}_x$ ) on downwind transects of the plume were used to determine OPE. Data from optical particle probes were used to study the time evolution of the aerosol size spectra. Box model calculations are used to show how OH and OPE vary as the plume evolves from a high  $\text{NO}_x$  to a low  $\text{NO}_x$  state.

## 2. Experimental

On Sunday, 10 September 2000, the G-1 sampled in the plume of the Sandow power plant during 12 successive downwind transects across the power plant plume over a 1-h period corresponding to <1–63 km downwind from the stack. Within several km of the stacks, the pilots were able to navigate by reference to visual plume boundaries. Navigation further downwind was done on the basis of real-time concentration measurements. The aircraft flew at a constant speed of  $100 \text{ m s}^{-1}$  as it repeatedly crossed the plume from 14:30 to 15:40 CST. A constant pressure altitude was maintained corresponding to 590 m (roughly 450 m above the terrain). After the last perpendicular pass through the plume, the plane turned directly toward the plant and returned over the stack while climbing steadily to above the boundary layer top in order to characterize the mixing height.

## 3. Instruments and methods

Winds aloft were calculated from the true air speed, measured with the G-1 gust probe, and the aircraft azimuth and ground track, measured with a TANS-Vector GPS receiver (Model 3000, Trimble Navigation Limited, Sunnyvale, CA). The resulting wind velocity scalars are estimated to have a standard deviation  $<0.5 \text{ m s}^{-1}$  for a 1-s time resolution.

The concentration of  $\text{SO}_2$  was measured using a pulsed fluorescence detector (Model 43S, Thermo Electron Corporation, Franklin, MA) with enhanced flow and modified electronics to increase the response speed (Nunnermacker et al., 1998). Ambient air was

Table 1  
Emissions and  $\text{NO}_x/\text{SO}_2$  ratio

Emission inventory (kton yr <sup>-1</sup> )		Molar ratio ( $\text{NO}_x/\text{SO}_2$ )	
$\text{SO}_2$	$\text{NO}_x$	Inventory	Observed
80,100	25,158	0.44	0.40 (0.05) <sup>1</sup>

<sup>1</sup> Average over traverses 4–12, with  $\text{SO}_2$  and  $\text{NO}_y$  corrected for deposition losses. (Standard deviation in parenthesis).

sampled by a forward-facing inlet situated in unperturbed air 20 cm from the fuselage. A continuous, 2-m length of 1-cm i.d., PFA tubing protruded slightly from the inlet and delivered air to the instrument inlet followed by an open-split into the unpressurized cabin. System sensitivity was checked every 2 h by standard addition in ambient air yielding a 30-ppbv signal on top of the ambient signal. The RMS noise was  $<0.2$  ppbv. The instrument was zeroed every 2 h through a  $K_2CO_3$  impregnated filter. At typical plume concentrations we estimate a  $1 - \sigma$  uncertainty of 10%. Time response is  $\sim 7$  s.

Ozone was measured using a modified commercial UV absorption detector (Model 49-100, Thermo Electron Corporation, Franklin, MA). The inlet manifold was identical to that described for  $SO_2$ . System sensitivity was checked every 1 h in flight against an internal  $O_3$  source which was standardized against a NIST-traceable NO standard by gas-phase titration at the beginning and end of the program. The instrument was zeroed every hour through an internal charcoal cartridge. The RMS noise for background air was  $<1$  ppbv.

$NO$ ,  $NO_2$  and total  $NO_y$  were measured using a 3-channel instrument designed and constructed at BNL. The instrument measures NO directly by detecting the chemiluminescence resulting from reaction with added  $O_3$ .  $NO_2$  is first converted to NO by photolytic reduction followed by detection as NO. NO and  $NO_2$  were delivered to the instrument via a PFA inlet as described above. Both sample streams passed through a 47-mm diameter, 1- $\mu$ m pore size Teflon filter at 1 SLPM.  $NO_y$  is quantified by reduction to NO in a Mo converter heated to 350 °C. The converter consists of  $\sim 10$  g of Mo mesh in a 1.3-cm i.d.  $\times$  15-cm length quartz tube. The tube and heater are contained in an airfoil-contoured pylon and the inlet protrudes slightly from the flat outboard end of the pylon. A  $\sim 1$ -mm pinhole on the rounded tip of the inlet is situated in the free air stream. Calibration standards of NO and  $NO_2$  are added to the ambient sample just inside the pinhole inlet. Total distance from the free air stream to the heated Mo mesh is  $<1$  cm. The system sensitivity and background were regularly measured in flight for all three channels. Sensitivity was checked by standard addition of NO. Converter efficiencies for both the photolysis cell ( $x = 0.348, \sigma = 0.005$ ), and the Mo converter ( $x = 0.996, \sigma = 0.003$ ) were assessed by partially titrating a fraction of the NO standard with  $O_3$ . The zero background was measured every 10 min by prereacting the ambient air with reagent  $O_3$ . Laboratory tests demonstrate a conversion efficiency for  $HNO_3$  of 90–95% in dry air and a 95% response time of 7 s to an instantaneous change in  $HNO_3$ .

A TSI 3010 condensation particle counter (Thermal Systems Inc., Shoreview, MN) was used to determine the number concentration of aerosol particles with

$D_p > 10$  nm. Size distributions of accumulation-mode particles were measured by optical light scattering in 15 size bins ranging from  $D_p = 0.1$ – $3 \mu$ m (PCASP-100X, Particle Measuring System, Inc., Boulder, CO). Coarse-mode particles were measured by optical light scattering in 15 size bins ranging from  $D_p = 0.5$ – $8 \mu$ m (FSSP-100, Particle Measuring System, Inc., Boulder, CO). Both probes were operated in flight with the de-icing heater on at all times. Probes were calibrated against polystyrene microspheres by the manufacturer prior to the field campaign. Size bins of the PCASP were corrected for the difference in refractive index between polystyrene ( $m = 1.59$ ) and ambient aerosol, which was assumed to be dry  $(NH_4)_2SO_4$  ( $m = 1.52$ ), using the response curves of Liu and Daum (2000). PCASP volume determined using the corrected size bins is about 20% greater than the uncorrected value. The uncertainty in aerosol number concentration and volume over the PCASP size range is qualitatively estimated as 20 and 50%, respectively, based on aircraft intercomparison flights using similar instrumentation (Moore II et al., 2004). The determination of aerosol volume from the FSSP is problematic because Mie resonances (particularly in the range  $D_p = 1$ – $4 \mu$ m) do not allow the unique association between a scattering signal and a particular size particle (Leaitch and Isaac, 1991; Jaenicke and Hanusch, 1993). Because of low concentrations of coarse mode particles a several minute averaging time was required to assemble reasonable statistics. Concentrations of the major inorganic ionic constituents of accumulation mode aerosols were determined from a PILS-IC (particle into liquid sampler-ion chromatography) with 3 min time resolution (Lee et al., 2003).

All real-time data were recorded on a single data system (M200, Science Engineering Associates, Willington, CT) at 1 Hz. We use the 1-s data for all subsequent analyses. To compare data between different analyzers, the raw data were adjusted in time to compensate for lags due to inlet residence, instrument mixing volumes, and electronic signal averaging. A constant time offset was determined for each system by comparing the signal to the 1-s data from the PCASP probe during transects of narrow features in an urban environment. While this procedure does not compensate for the smoothing of rapidly changing signals by slow instruments, it allows more direct comparison of fast signals (such as NO:  $\tau = 2$  s and particles:  $\tau < 1$  s) with slower signals (such as  $SO_2$ :  $\tau = 7$  s and  $O_3$ :  $\tau = 9$  s).

## 4. Results and observations

### 4.1. Meteorology

Widespread precipitation and relatively cool air moved through the region on 9 September the day

before this flight. Air flow was southeasterly over the Houston area bringing clouds and moisture in from the Gulf of Mexico. Weather on the flight day was mostly clear with scattered cumulus. During the transects, at a constant altitude of 590 m, the static temperature increased from 27.7 to 29.5 °C. The water vapor mixing ratio varied between 13 and 14 g kg<sup>-1</sup> corresponding to a relative humidity of 50%. The boundary layer top at 15:50 was at an altitude of 1820 m as indicated by a temperature inversion measured during the climb out of the plume at the end of sampling. Scattered cumulus clouds were widely distributed at or just above the boundary layer. Except for this, the entire mission was flown in cloud-free air.

The vector-averaged wind over the straight and level flight portions of all plume transects was 3.8 ( $\sigma_{1s} = 1.2$ ) m s<sup>-1</sup> at 142 ( $\sigma_{1s} = 24$ )°. We observed no systematic changes in the wind speed or direction measured aloft at 590 m during plume sampling. Surface winds at Continuous Air Monitoring Station #601 (EPA site number: 48-149-0001) operated by Air Quality Solutions for the Lower Colorado River Authority in neighboring Fayette County were steady at 2.3 m s<sup>-1</sup> at 170° during the flight period, changing from a slightly more southerly direction in the 3 h preceding the flight. Plume age as a function of location was determined as the straight-line distance from the stack divided by the mean wind velocity. The rural area beneath the plume, both immediately upwind and downwind, was relatively free of point sources and major transportation arteries as determined by emissions maps and observations. Background levels of primary pollutants immediately upwind of the source and outside the plume edges were low, e.g.; O<sub>3</sub> = 55–60 ppbv, NO<sub>x</sub> = 0.6 ppbv, and SO<sub>2</sub> = 0.3 ppbv.

#### 4.2. Chemical measurements

Of the trace gases observed from the G-1, SO<sub>2</sub> is closest to being a zero-background conservative tracer and is therefore used to produce a picture of the spatial extent of the plume. An SO<sub>2</sub> time series is shown in Fig. 1 with measurements in the plume distinguished by the shaded bands. The 12 traverses are labeled in order of increasing downwind distance. A two-dimensional picture of the plume superimposed over the flight track is shown in Fig. 2. The path of the plume is consistent with measurements from the Fayette County ground station showing steady southerly winds changing to SSE ~2 h prior to plume sampling. An age is assigned to each traverse based on the downwind distance from the stack and the average wind velocity. Calculated plume ages range from 0.2 to 4.6 h. Subtracting these ages from the time each leg was flown yields the time of emission, ranging from 14:20 for the first leg to 11:00 for the 12th leg. Legs 9–12 were exposed to solar noon while the other legs received correspondingly less intense

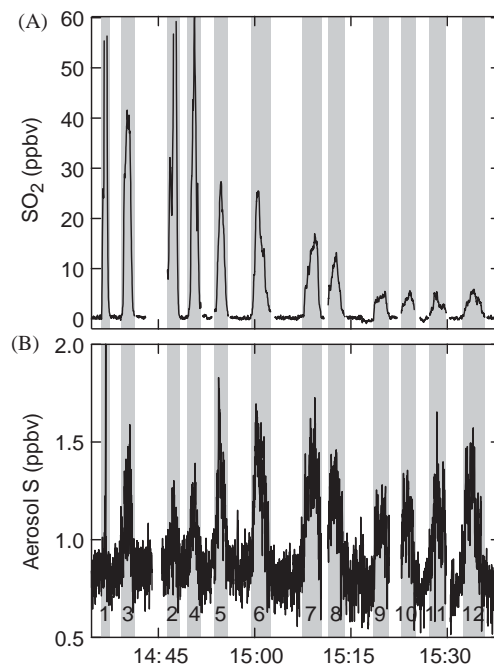


Fig. 1. Concentration of SO<sub>2</sub> and SO<sub>4</sub><sup>2-</sup> vs. time with plume transects numbered in order of increasing downwind distance as shown in Fig. 2. Aerosol SO<sub>4</sub><sup>2-</sup> calculated from PCASP size distributions assuming a composition of dry, spherical (NH<sub>4</sub>)<sub>2</sub>SO<sub>4</sub>.

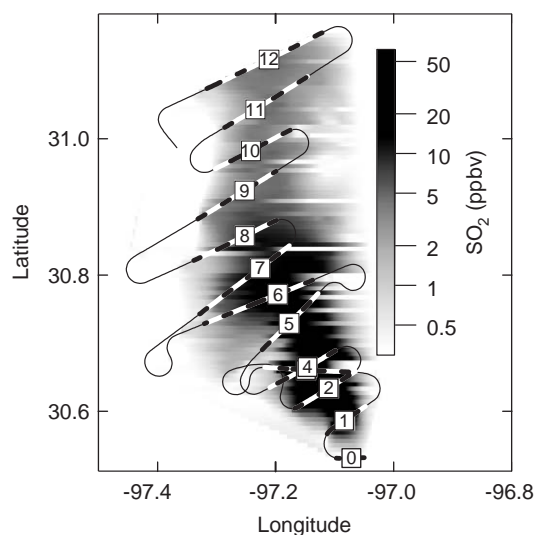


Fig. 2. Ground track of G-1 aircraft showing gridded SO<sub>2</sub> concentration generated from time series data shown in Fig. 1. Plume transects are numbered in order of increasing downwind distance. Dashed portions are considered in plume and correspond to shaded regions in Figs. 1, 3 and 4.

irradiation. Using these ages, various processing rates can be determined.

Fig. 1 also shows the aerosol  $\text{SO}_4^{2-}$  concentration as calculated from PCASP size distribution measurements assuming that all of the aerosol above background in the plume is  $(\text{NH}_4)_2\text{SO}_4$ . No adjustments due to relative humidity were made to the sizing data as the sample is dried by both the deicing heater in the optical probe and adiabatic heating from compression. Data from the PILS-IC instrument, although limited by its 3-min time resolution, yield an average  $\text{NH}_4^+$ -to- $\text{SO}_4^{2-}$  molar ratio of 2.5, indicating complete neutralization. A comparison of Figs. 1A and B shows that  $\text{SO}_4^{2-}$  (as calculated from aerosol volume) increases monotonically relative to  $\text{SO}_2$ . Absolute  $\text{SO}_4^{2-}$  concentrations decrease slightly after transect 7 due to plume dispersion.

Fig. 3 shows a time sequence for  $\text{NO}_x$  and  $\text{NO}_y$ . The data in Fig. 3 have been scaled by 12% ( $\text{NO}_y$  increased) so that the ratio of  $\text{NO}_x$  to  $\text{NO}_y$  is unity at the emission source. This scaling factor is based on an observed ratio (cross-wind integrated values) of 1.03 at transect 4, corrected for oxidation of  $\text{NO}_x$  occurring between the source and transect 4 as described in a following section. The estimated  $1 - \sigma$  accuracy of the  $\text{NO}_x$  and  $\text{NO}_y$  measurements is 10%, so one would expect a  $1 - \sigma$  accuracy between 10 and 14% for  $\text{NO}_x/\text{NO}_y$  depending

on whether errors are common or independent. At the furthest downwind transects, the  $\text{NO}_x$ -to- $\text{NO}_y$  ratio becomes ill-defined because plume  $\text{NO}_x$  is not much larger than background. In contrast, Fig. 1 shows that  $\text{SO}_4^{2-}/\text{SO}_2$  retains a high signal-to-noise ratio far downwind.

Ozone concentrations are depicted in Figs. 4 (time series) and 5 (interpolated 2D-plot). Immediately downwind of the stack,  $\text{NO}$  emissions react with background ozone entrained in the plume causing a local reduction in  $\text{O}_3$ . Near the source, this titration with  $\text{NO}$  reduces the  $\text{O}_3$  concentration well below background levels to nearly zero. By transect 4, net  $\text{O}_3$  production occurs at the plume boundaries, where the  $\text{NO}_x$  concentration is low enough to allow rapid  $\text{O}_3$  production (Gillani et al., 1998; Ryerson et al., 1998). At a plume age of 1.5 h (transect 5), ozone production has overcome the initial loss and surplus ozone is evident across the plume. The magnitude

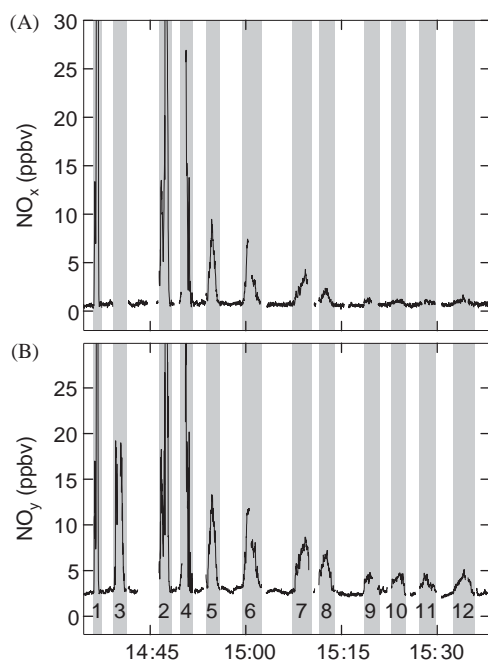


Fig. 3. Concentration of  $\text{NO}_x$  and  $\text{NO}_y$  vs. time with plumes transects numbered in order of increasing downwind distance.  $\text{NO}_y$  concentration incorporates a 12% increase as described in text.

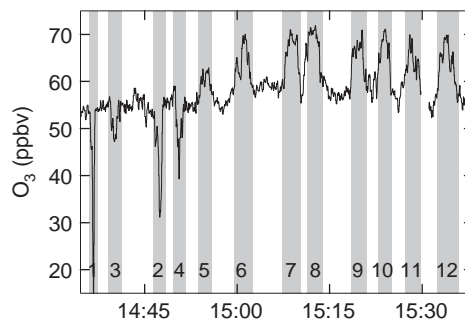


Fig. 4. Concentration of  $\text{O}_3$  vs. time with plume transects numbered in order of increasing downwind distance.

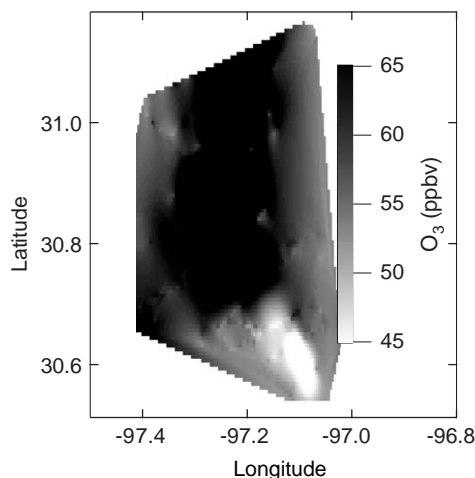


Fig. 5. Ground track of G-1 aircraft showing gridded  $\text{O}_3$  concentration generated from time series data shown in Fig. 4.



of ozone production is not fully apparent in Figs. 4 and 5 as dilution with background air increasingly masks the appearance of new ozone with plume age.

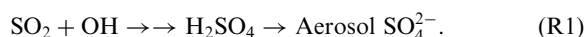
Table 1 shows that there is reasonable agreement between the S-to-N ratio obtained from the 1999 EPA emission inventory and that observed on 9 downwind traverses of the plume. We have not attempted to compare absolute values of emission fluxes because of the difficulty in determining this quantity from traverses at a single altitude. Qualitatively, it can be seen from Figs. 1 and 3 that the crosswind integrated concentrations (areas under the plume peaks) decrease significantly after traverses 8–9. It appears that vertical and/or horizontal diffusion has moved much of the plume outside of our sampling range. Sampling at multiple altitudes would be required to locate the remainder of the original emission. We recognize the displacement of the plume from the aircraft path and concentrate on comparing the ratios of various components to study transformation processes in the plume.

## 5. Plume chemistry

Within the power plant plume  $\text{SO}_2$  is oxidized forming aerosol sulfate,  $\text{NO}_2$  is oxidized to  $\text{HNO}_3$ , and  $\text{O}_3$  is produced. From a simple model of in-plume chemistry and deposition we derive 2 values for OH concentration and an  $\text{O}_3$  production efficiency. Changes in particle size distribution yield information on primary emissions and the aerosol formation processes.

### 5.1. Oxidation reactions and OH determination

As the emitted pollutants,  $\text{SO}_2$  and  $\text{NO}_x$ , are oxidized primarily by reaction with OH, the appearance of reaction products as a function of time can be used to estimate OH concentration. The plume oxidation reactions are:



R1 is a multistep reaction with  $\text{SO}_2 + \text{OH}$  being rate determining. We will assume that  $\text{NO}_2$  is proportional to  $\text{NO}_x$  and that  $\text{HNO}_3$  is the dominant  $\text{NO}_x$  oxidation product as has been established in other power plant studies. Dry deposition of  $\text{SO}_2$  and  $\text{HNO}_3$  occur at a fast enough rate that they should be taken into account. Loss by deposition can be expressed as



The deposition velocities for  $\text{SO}_2$  and  $\text{HNO}_3$  are estimated to be 0.5 and 3  $\text{cm s}^{-1}$ , respectively. Assuming

a well-mixed boundary layer with a measured depth of  $\sim 1700$  m, the rates of R3 and R4 (given by deposition velocity/depth) are 1.1 and 6.4%  $\text{h}^{-1}$ . Deposition of  $\text{NO}_x$  and aerosol sulfate is slower and will be ignored. The other significant process affecting chemical concentrations is plume dispersion. In the following equations we end up using only the ratios of concentrations which are not affected by dispersion.

Reactions 1–4 lead to first-order differential equations describing the time dependence of  $\text{SO}_2$ , aerosol  $\text{SO}_4^{2-}$ ,  $\text{NO}_x$ , and  $\text{HNO}_3$ :

$$d\text{SO}_2/dt = -k_1\text{OH SO}_2 - k_3\text{SO}_2 \quad (1)$$

$$d\text{SO}_4^{2-}/dt = k_1\text{OH SO}_2 \quad (2)$$

$$d\text{NO}_x/dt = -k_2f\text{OH NO}_x \quad (3)$$

$$d\text{HNO}_3/dt = k_2f\text{OH NO}_x - k_4\text{HNO}_3, \quad (4)$$

where  $f = \text{NO}_2/\text{NO}_x$ . The value of  $f$  varies from transect to transect, in response to changing  $\text{O}_3$ ,  $\text{NO}_x$ , and sunlight and exhibits a general increase as the  $\text{NO}_x$  concentration decreases. We estimate that  $f = 0.85$  based on observations from the middle transects. Eqs. (1)–(4) have the solution

$$\text{SO}_2(t) = \text{SO}_2(0) \exp(-k_s t),$$

$$k_s = (k_1\text{OH} + k_3), \quad (5)$$

$$\text{SO}_4^{2-}(t) = \text{SO}_2(0)\alpha(1 - \exp(-k_s t)),$$

$$\alpha = k_1\text{OH}/(k_1\text{OH} + k_3), \quad (6)$$

$$\text{NO}_x(t) = \text{NO}_x(0) \exp(-k_2f\text{OH}t), \quad (7)$$

$$\text{HNO}_3(t) = \text{NO}_x(0)\beta[\exp(-k_4t) - \exp(-k_2f\text{OH}t)],$$

$$\beta = k_2f\text{OH}/(k_2f\text{OH} - k_4). \quad (8)$$

Eqs. (5)–(8) were used to construct the quantities,  $\ln(1 - \text{SO}_4^{2-}/(\text{SO}_2 + \text{SO}_4^{2-}))$  and  $\ln(\text{NO}_x/\text{NO}_y)$  which depend only on time, rate constants,  $f$ , and OH concentration. The corresponding observed quantities are determined from cross-plume integrated concentrations above background of  $\text{SO}_2$ ,  $\text{SO}_4^{2-}$ ,  $\text{NO}_x$ , and  $\text{NO}_y$  (see Figs. 1 and 3). The  $\text{SO}_4^{2-}$  above background is determined from the PCASP using size bins smaller than  $D_p = 0.4 \mu\text{m}$ . Plume concentrations of larger particles could not be reliably distinguished from background values outside of the plume. A non-linear least squares program yields the OH concentration that minimizes the deviation of these OH dependent functions from the corresponding observed quantities. By neglecting the dependence of OH on downwind distance, Eqs. (1)–(8) yield an average OH that pertains to chemical conversion over the time period that the plume was sampled. Departures from that average are discussed below.

Kinetic plots are shown in Fig. 6. For sulfur chemistry, 11 of 12 traverses were used. Traverse 3 was not used because the plume was crossed at an acute angle causing a spread in downwind distance. For  $N$  chemistry an additional 2 traverses, 1 and 2, were not used because of rapidly changing and out-of-range concentrations. The fraction of  $SO_2$  oxidized at transect 4 is 0.008.  $NO_x$  oxidation is 11.6 times faster than  $SO_2$  ( $k_2/k_1 = 9.94 \times 10^{-12}/8.57 \times 10^{-13}$ ; Sander et al., 2003) implying that the fraction of  $NO_x$  oxidized is 0.09. Our 12% adjustment factor for  $NO_x/NO_y$  is based on a 9% extrapolation of the observed  $NO_x/NO_y$  (1.03) at transect 4 back to zero time. This adjustment is within measurement uncertainty and is necessary to give a 100%  $NO_x$  plume at  $t = 0$ . Note that in both the S and N plots, oxidation starts out slow as would be expected for a high  $NO_x$  environment with suppressed photochemistry. The OH concentrations determined with and without dry deposition are given in Table 2. With deposition taken into account, OH concentrations are  $8.0$  and  $11 \times 10^6 \text{ cm}^{-3}$  from  $SO_2$  and  $NO_x$  kinetics, respectively. Uncertainties for OH levels based on linear regression statistics are  $\pm 5 \times 10^5 \text{ cm}^{-3}$  from  $SO_2$

oxidation and  $\pm 8 \times 10^5 \text{ cm}^{-3}$  from  $NO_x$  oxidation. These uncertainties do not include possible systematic measurement biases which are included in the error bars shown in Fig. 6. These error bars were calculated using instrument uncertainties (10, 10, 10, and 50%, for  $NO_x$ ,  $NO_y$ ,  $SO_2$ , and  $SO_4^{2-}$ , respectively) plus an estimate for imprecisely known background concentrations which have to be subtracted from the plume measurements (0.15, 0.2, 0.3, and 0.1 ppbv for  $NO_x$ ,  $NO_y$ ,  $SO_2$ , and  $SO_4^{2-}$ , respectively). Background uncertainty was determined as the low frequency variability of the out-of-plume portion of each transect. Uncertainties are combined in quadrature under the assumption that they are independent. Errors in estimating  $SO_2$  oxidation are dominated by the uncertainty in PCASP bin size which contributes most of the 50% uncertainty of the volume measurements. Close to the power plant most of the uncertainty in  $NO_x$  conversion is due to the difficulty of measuring  $NO_z$  as the small difference between 2 large numbers. Further downwind, background subtraction becomes the largest source of uncertainty.

Fig. 7 compares  $SO_2$  and  $NO_x$  oxidation amounts following a method used by Brock et al. (2002, 2003). A calculated curve is shown, determined from OH kinetics and deposition, using an OH concentration that is the average of that obtained for  $SO_2$  and  $NO_x$  oxidation, i.e.,  $OH = 9.6 \times 10^6 \text{ molecule cm}^{-3}$ . Note that the calculated curve depends on OH concentration only in so far as deposition competes with oxidation. There is qualitative agreement between the calculated curve and the data points, consistent with the  $1 - \sigma$  error estimates. Almost all of the discrepancy is caused by observations on transects 7–10. However, there are no obvious distinctive attributes of those transects.

## 5.2. Ozone production efficiency

A useful metric for the  $O_3$ -forming potential of  $NO_x$  emissions is the OPE (Trainer et al., 1993), defined here as the number of molecules of oxidant ( $O_3 + NO_2$ ) formed per molecule of  $NO_x$  oxidized. We calculate this quantity for each transect as the slope of a graph of  $O_x$  vs.  $NO_z$ . Two such regression plots are illustrated in

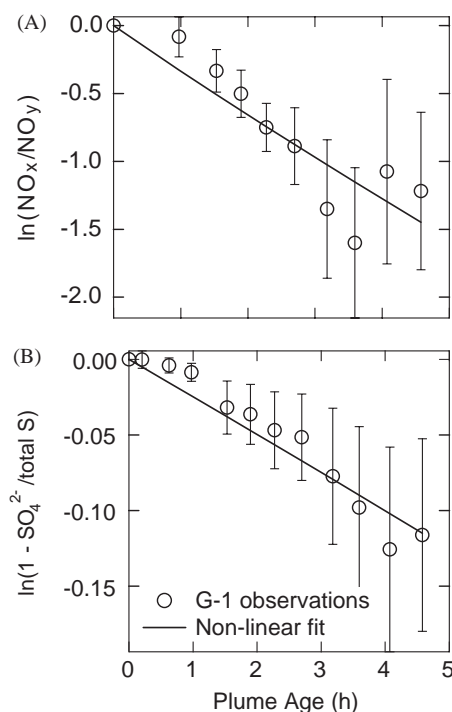


Fig. 6. Kinetic plots used to determine OH concentration from (A) oxidation of  $NO_x$  and (B) oxidation of  $SO_2$ . Error bars give  $\pm 1\sigma$  uncertainties as described in text. Non-linear least-squares fit is based on Eqs. (5)–(8) describing oxidation process and deposition of  $SO_2$  and  $HNO_3$ . OH concentrations so derived are given in Table 2.

Table 2  
OH concentration from  $SO_2$  and  $NO_x$  oxidation kinetics

Method	OH concentration ( $\text{cm}^{-3}$ )		OH ratio: $NO_x/SO_2$
	$SO_2$ oxidation	$NO_x$ oxidation	
With deposition	$7.96 \times 10^6$	$1.13 \times 10^7$	1.42
Without deposition	$8.09 \times 10^6$	$1.05 \times 10^7$	1.30

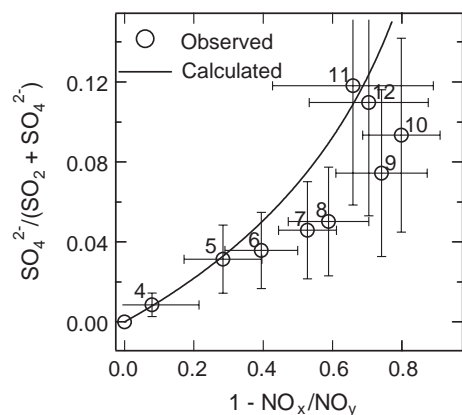


Fig. 7. Fraction of  $\text{SO}_2$  oxidized to  $\text{SO}_4^{2-}$  vs. fraction of  $\text{NO}_x$  oxidized to  $\text{NO}_2$  for 9 traverses of the Sandow plume. Error bars give  $1 - \sigma$  uncertainties as described in text. Curved line is the calculated relation between  $\text{SO}_2$  and  $\text{NO}_x$  oxidation for an OH concentration of  $9.6 \times 10^6 \text{ molecules cm}^{-3}$ , an  $\text{NO}_2$  to  $\text{NO}_x$  ratio of 0.85, and deposition velocities of  $\text{SO}_2$  and  $\text{HNO}_3$  of 0.5 and  $3 \text{ cm s}^{-1}$ , respectively.

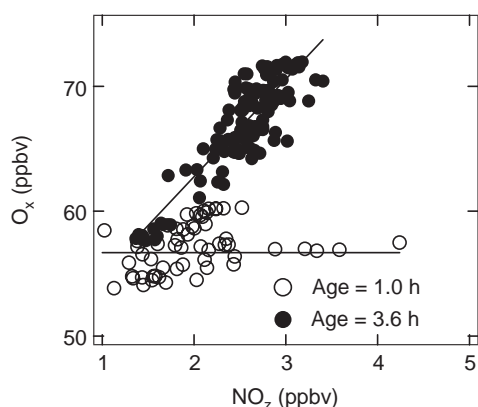


Fig. 8. Typical  $\text{O}_x$  ( $\text{O}_3 + \text{NO}_2$ ) vs.  $\text{NO}_2$  ( $\text{NO}_y - \text{NO}_x$ ) scatter plots shown here for traverses 4 and 10. Data points are from 1-s measurements. Lines are linear least-squares fit for each traverse. Slope gives an ozone production efficiency.

Fig. 8. Fig. 9 shows the change in OPE as a function of processing time. OPE is seen to be low in the high  $\text{NO}_x$  environment near the stack, increasing to 5–6 on the furthest downwind transects.

### 5.3. Aerosol concentration and size spectra

Particle size distributions are used here to characterize changes to the aerosol population due to primary emissions and gas-to-particle conversion. Figs. 10 and 11 depict aerosol number and volume size distributions over the size range covered by the PCASP (0.1–3  $\mu\text{m}$ ) and

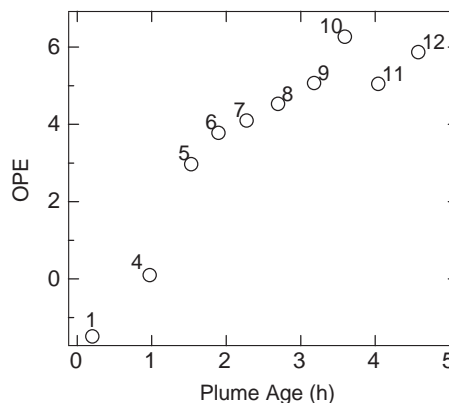


Fig. 9. Ozone production efficiency (OPE) determined as the slope of a plot of  $\text{O}_x$  ( $\text{O}_3 + \text{NO}_2$ ) vs.  $\text{NO}_2$  ( $\text{NO}_y - \text{NO}_x$ ) for 10 traverses of the Sandow plume. Results presented as a function of plume age with data points labeled by traverse number.

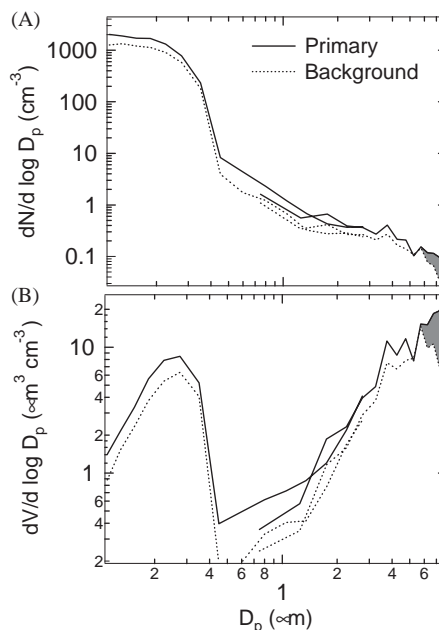


Fig. 10. Aerosol size distribution in the near-stack environment and in background air. Regions defined in Table 3. Panel (A) shows number size distribution  $dN/d \log D_p$  vs.  $\log D_p$ . Panel (B) shows volume size distribution  $dV/d \log D_p$  vs.  $\log D_p$ . PCASP covers the size range 0.1–3  $\mu\text{m}$ ; FSSP from 0.5 to 8  $\mu\text{m}$ . Filled area indicates an increase in coarse particles in near-stack environment, relative to background.

FSSP (0.5–8  $\mu\text{m}$ ) for data subsets representing the near stack environment and the mature plume, respectively. In each graph we include a spectrum of unperturbed background air. In all three environments, particle spectra show prominent accumulation and coarse particle modes, with a deep minimum in between. Because



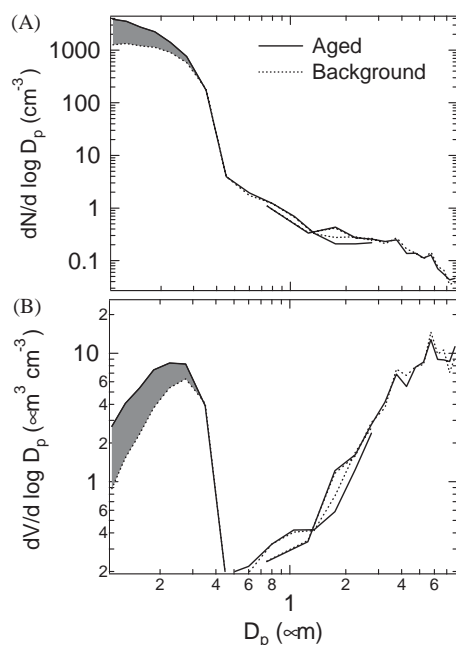


Fig. 11. Aerosol size distribution in the mature plume and in background air. Regions defined in Table 3. Format same as Fig. 10. Filled area indicates an increase in accumulation mode particles in mature plume, relative to background.

concentrations of large particles are low, results have been averaged over several minutes. In the overlap region,  $D_p$  between 0.5 and 3  $\mu\text{m}$ , there is good agreement between FSSP and PCASP particle number concentration and volume. However, larger disagreements are not uncommon because of the multivalued relation between particle size and scattering in the FSSP (Leaith and Isaac, 1991). Number and volume concentrations are summarized in Table 3.

Most of the particles, by number concentration, are in the Aitken mode with  $D_p$  smaller than 0.1  $\mu\text{m}$ , below the detection threshold of the PCASP. Background concentrations of CNC ( $D_p > 10 \text{ nm}$ ) were  $2000 \text{ cm}^{-3}$ . Emissions from the Sandow stacks add large numbers of small particles. Peak concentrations observed on the close-in transects were approximately  $10^5 \text{ cm}^{-3}$ . Fig. 12 shows the number concentration of particles with  $D_p > 10 \text{ nm}$  and  $D_p > 0.1 \mu\text{m}$ , normalized to the concurrently measured concentration of  $\text{SO}_2$  which we use as tracer to account for plume dispersion. To a first approximation, the total number of particles ( $D_p > 10 \text{ nm}$ ) per ppbv  $\text{SO}_2$  is constant after transect 1. Assuming that  $\text{SO}_2$  is a conservative tracer, this implies that the total number of particles in the plume is fixed. In contrast, the number of accumulation mode particles ( $D_p > 0.1 \mu\text{m}$ ) per ppbv  $\text{SO}_2$  increases two orders of magnitude as gas-to-particle conversion causes smaller particles to grow into the range detected by the PCASP

Table 3

Observed aerosol number and volume concentrations

Region <sup>1</sup>	PCASP	FSSP/ PCASP	FSSP
	0.1–3 $\mu\text{m}$	0.5–3 $\mu\text{m}$	0.5–8 $\mu\text{m}$
Average number concentration ( $\text{cm}^{-3}$ )			
Background	528	0.84	0.55
Near-stack	769	0.60	0.82
Mature plume	1151	0.81	0.54
Average volume concentration ( $\mu\text{m}^3 \text{ cm}^{-3}$ )			
Background	2.81	1.06	4.10
Near-stack	4.05	0.98	6.24
Mature plume	3.98	1.22	3.98

Near-stack ( $\text{SO}_2 > 30 \text{ ppbv}$ ), 168 s data.

Mature plume (traverses 8–12;  $N_{\text{PCASP}} > 1000 \text{ cm}^{-3}$ ), 346 s data.

<sup>1</sup>Background ( $\text{SO}_2 < 0.75 \text{ ppbv}$ ;  $N_{\text{PCASP}} < 600 \text{ cm}^{-3}$ ), 1306 s data.

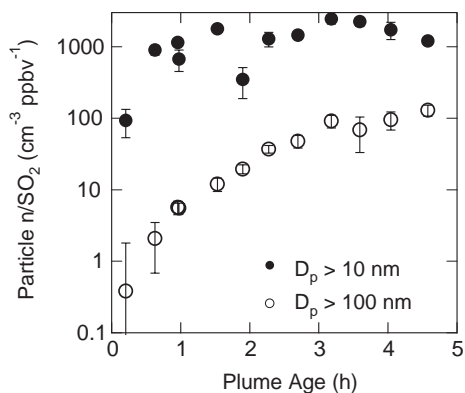


Fig. 12. Number concentration of particles with  $D_p > 10 \text{ nm}$  and  $D_p > 0.1 \mu\text{m}$ , normalized to concurrently measured  $\text{SO}_2$ , as a function of plume age. Ratio of particle to  $\text{SO}_2$  concentration determined from a linear least-squares regression. Error bars are uncertainty estimate of regression slope.

(see below). The absolute number concentration of accumulation mode particles increases 2-fold in the 4.6-h plume lifetime despite the effects of dilution.

The near-stack size spectra show an increase in number and volume concentration relative to background, with the largest changes occurring in the accumulation mode and at the large size end of the coarse particle mode. The accumulation mode increase is partly due to secondary aerosol, i.e. condensation of  $\text{H}_2\text{SO}_4$ , as it is observed to increase with time within the near-stack environment. In contrast, the near-stack coarse particle increase is only due to primary emissions as there is no mechanism to create this size particle in the atmosphere. We have tested the statistical significance of the excess FSSP volume observed in the near-stack

region with a Monte Carlo calculation, finding that no more than a few percent can be attributed to chance.

The relation between  $\text{SO}_2$  and FSSP volume for all transects is shown in Fig. 13 where data have been binned into 4 categories according to  $\text{SO}_2$  concentration. The intercept of a linear least-squares fit to the averaged data indicates a background FSSP volume of  $4.7 \mu\text{m}^3 \text{m}^{-3}$  in reasonable agreement with background coarse particle volume presented in Table 3. Coarse particle volume associated with plume  $\text{SO}_2$  given by the slope of the regression line is  $0.06 \mu\text{m}^3 \text{m}^{-3}$  per ppbv  $\text{SO}_2$ . Assuming a density range of  $1\text{--}2 \text{ g cm}^{-3}$  for fly ash, the weight ratio of primary coarse particles to  $\text{SO}_2$  is  $0.02\text{--}0.04$ , 2–4 times greater than the 0.011 ratio determined from the 1999 EPA inventory as  $(\text{PM}_{10}\text{--PM}_{2.5})/\text{SO}_2$ . Most of the primary coarse particle volume is in the  $6\text{--}8\text{-}\mu\text{m}$  size bins (Fig. 10B). Presumably there is additional volume above the  $8\text{-}\mu\text{m}$  cutoff of the FSSP, which would cause the discrepancy with the emission inventory to be greater than a factor of 2–4. It is difficult to assign an uncertainty to these figures because the response of the FSSP to nonspherical fly ash particles has not been quantified.

In the mature plume (Fig. 11), excess aerosol relative to background appears only in the size range  $0.1\text{--}0.3 \mu\text{m}$ , with a 3-fold increase of particles in the smallest size bin,  $0.1\text{--}0.12 \mu\text{m}$ . In the  $0.1\text{--}0.3\text{-}\mu\text{m}$  size range, a growth law analysis such as described by McMurray et al. (1981), and used by Brock et al. (2002) in a recent study of power plant plumes shows that the size dependence of excess aerosol is consistent with a condensational growth mechanism. The dominant feature of the PCASP spectrum in the mature plume is therefore particles

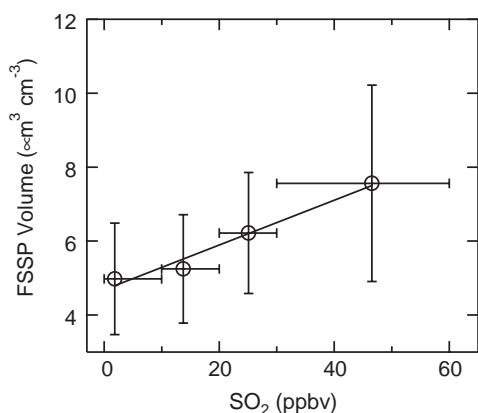


Fig. 13. Coarse particle volume determined from the FSSP vs.  $\text{SO}_2$  concentration. Data from the Sandow plume has been averaged over 10 s intervals and binned by  $\text{SO}_2$  concentration. Standard deviation of FSSP volume and range of  $\text{SO}_2$  concentration within a bin are indicated by error bars. Straight line is a linear least-squares fit to the averaged data points.

growing into the observable range by vapor deposition of  $\text{H}_2\text{SO}_4$ . However, neither a condensational mechanism nor a volume growth mechanism can explain the observation that particles with  $D_p > 0.3 \mu\text{m}$  remain at background levels. Although this by itself does not totally explain the discrepancy, we note that the PCASP instrument can missize particles in the  $0.35\text{--}0.65\text{-}\mu\text{m}$  range due to Mie scattering resonances, and that size bins in this range are sometimes lumped together (Leitch et al., 1991).

## 6. Discussion

As a qualitative test of OH concentrations and  $\text{O}_3$  production efficiencies inferred from plume observations, we have done photochemical model simulations of conditions in the Sandow plume. A model of plume transport and chemical transformation requires more detailed meteorological information to determine dispersion than is available, so instead we have conducted a series of constrained steady-state (CSS) box model calculations meant to describe the chemistry at various points in the plume's time evolution. Given a set of concentrations for stable long-lived species this model solves the photochemical kinetic rate equation yielding the concentration of OH as well as the production and loss rates for  $\text{O}_3$  and  $\text{NO}_x$  (Kleinman et al., 2002). Concentrations of stable species which are not primary pollutants are specified as the average of observations made at 2 locations, one outside of the plume on transect 5 and one in a dilute region on transect 10, where hydrocarbon samples were collected. Model parameters are summarized in Table 4. Air outside of the plume is seen to have low VOC reactivity. Photolysis rates were calculated on the basis of 72% of the solar intensity at 14:00—a representative mid-point for the air parcels that we sampled in, which were emitted earlier in the day.

In order to simulate conditions in the plume,  $\text{NO}_x$  was varied from near zero to 50 ppbv and  $\text{SO}_2$  was varied in proportion to  $\text{NO}_y$ . Plume  $\text{SO}_2$  has a minor effect on OH, causing a 5% reduction in peak values. The effect on  $\text{P}(\text{O}_3)$  and OPE is larger: a 5–10% increase under low  $\text{NO}_x$  conditions and an even larger increase in the high  $\text{NO}_x$ , VOC limited region near the stack. Changes to  $\text{P}(\text{O}_3)$  are a result of  $\text{SO}_2$  acting like a VOC in that the reaction with OH produces an  $\text{HO}_2$  peroxy radical (Stockwell, 1994). Calculations indicate that the effects of CO (observed) and hydrocarbon emissions from Sandow (determined from the EPA emission inventory) were not significant. Fig. 14 shows calculated OH as a function of  $\text{NO}_x$  concentration. A low OH concentration and therefore a slow  $\text{NO}_x$  oxidation rate in the high  $\text{NO}_x$  environment near the source (Karamchandani and Seigneur, 1999) is in agreement with the kinetic data

Table 4  
Inputs to photochemical box model calculation

Parameter	Value
Time	14:00 LST
O <sub>3</sub>	61 ppbv
CO	125 ppbv
NO <sub>x</sub>	variable: 0.1–50 ppbv
SO <sub>2</sub>	variable: 0.01–135 ppbv
Anthropogenic hydrocarbon OH reactivity	0.17 s <sup>-1</sup>
Biogenic hydrocarbon OH reactivity	0.09 s <sup>-1</sup>
CH <sub>4</sub>	1830 ppbv
HCHO	2.6 ppbv
H <sub>2</sub> O <sub>2</sub>	3.4 ppbv
ROOH	5.1 ppbv
solar intensity	72% of clear sky

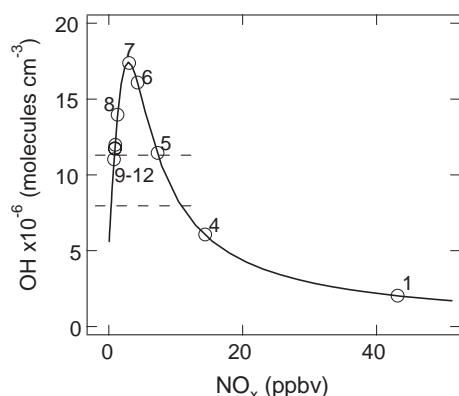


Fig. 14. OH concentration calculated from CSS box model as a function of NO<sub>x</sub> concentration (smooth curve). Model inputs are from Table 4 except for NO<sub>x</sub> and SO<sub>2</sub> which were varied to simulate the range of plume concentrations. Data points are placed on calculated curve according to the average NO<sub>x</sub> concentration observed on the individual traverses. Dashed lines indicate OH concentrations determined from SO<sub>2</sub> and NO<sub>x</sub> oxidation kinetics (see Table 2).

presented in Fig. 6. Dashed lines in Fig. 14 show the range of OH concentration deduced from SO<sub>2</sub> and NO<sub>x</sub> oxidation. These OH concentrations are seen to be near the average OH experienced by an air parcel as it evolves from the high NO<sub>x</sub> concentration of transect 1 to the sub-ppbv NO<sub>x</sub> concentrations in transects 9–12. We take this as qualitative evidence ( $\sim \pm 50\%$ ) of the soundness of the kinetic analysis.

The net production rate of O<sub>3</sub>,  $P_N(O_3)$ , and OPE were also determined as a function of NO<sub>x</sub> from the CSS calculations, as shown in Fig. 15. For NO<sub>x</sub> concentrations greater than 10 ppbv, O<sub>3</sub> production is slow,

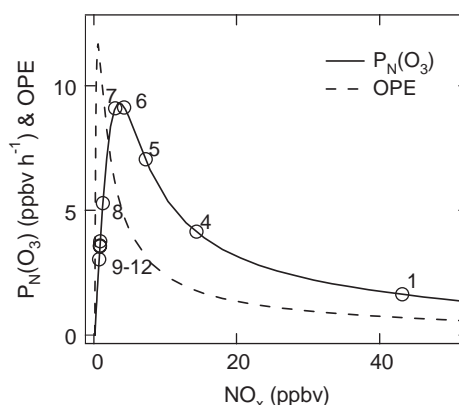


Fig. 15. Net ozone production rate,  $P_N(O_3)$ , and ozone production efficiency, OPE, as a function of NO<sub>x</sub> concentration from the same set of box model calculations used in Fig. 14.  $P_N(O_3)$  is the difference between O<sub>3</sub> chemical production and loss.  $OPE = P(O_3)/P(NO_2)$ , where  $P(O_3)$  is the rate of O<sub>3</sub> production and  $P(NO_2)$  is the rate of NO<sub>2</sub> production, i.e., the rate of NO<sub>x</sub> oxidation. As in Fig. 14, data points on calculated curve indicate the average NO<sub>x</sub> concentration observed on a traverse.

$< 6 \text{ ppbv h}^{-1}$ , and inefficient,  $OPE < 2$ . This is due to a low VOC to NO<sub>x</sub> ratio caused by the absence of significant quantities of biogenic or anthropogenic hydrocarbons. At lower NO<sub>x</sub> concentration both  $P_N(O_3)$  and OPE increase. Ozone production rates and efficiencies presented in Fig. 15 are instantaneous values based on local conditions. OPE determined from measurements (Figs. 8–9), in contrast, depends on O<sub>3</sub> production and NO<sub>x</sub> oxidation over the time span from emissions to measurement. Furthermore, the measured OPE is not a simple time integral of the instantaneous OPE over the time history of the emitted air parcel, so the comparison between Figs. 9 and 15 is only qualitative. Still there are a few features worth noting. The negative OPE on the first transect of Fig. 9, in part reflects the difficulty of calculating NO<sub>2</sub> as the difference between NO<sub>x</sub> and NO<sub>y</sub> when the fraction of conversion is very low. However, OPEs as negative as  $-1$  are physically allowed. Suppose the instantaneous OPE has a constant value of  $n$ , i.e. reaction produces  $n$  molecules of O<sub>3</sub> for each molecule of NO<sub>x</sub> oxidized. Then for each molecule of NO<sub>x</sub> oxidized, the concentration of O<sub>x</sub> is reduced by loss of one NO<sub>2</sub> and increased by the production of  $n$  molecules of O<sub>3</sub> resulting in a net increase of  $n - 1$  molecules of O<sub>x</sub> (Kleinman et al., 2002). An instantaneous OPE close to 1 in the high NO<sub>x</sub> area near transect 1 implies that the measured (i.e., time averaged) OPE should be near zero, as is observed. Beyond transect 4, the instantaneous OPE increases rapidly reaching a maximum value of almost 12 near transect 12. This is also a region of high O<sub>3</sub> production

rates and the measured OPE of 5–6 in this region reflects the O<sub>3</sub> that was formed under low NO<sub>x</sub> conditions.

## 7. Conclusions

Aerosol and trace gas measurements were made on 10 September 2000, during 12 transects of the lignite fired Sandow power plant plume. These transects span a 4.6 h plume lifetime centered near local noon. The appearance of aerosol SO<sub>4</sub><sup>2-</sup> and the conversion of NO<sub>x</sub> to oxidation products as a function of atmospheric processing time yields average OH concentrations of 8.0 and 11 × 10<sup>6</sup>, respectively. These estimates agree with each other within uncertainty limits. Particle size spectra determined with a PCASP are consistent with the addition of SO<sub>4</sub><sup>2-</sup> mass by condensation onto Aitken and accumulation mode size particles. Primary emissions of coarse particles (> 5 μm) were observed. Ozone production was seen on downwind traverses but high O<sub>3</sub> concentrations were not reached because of extensive plume dilution. Ozone production efficiencies varied from near zero close to the stack to 5–6 on downwind low-NO<sub>x</sub> traverses. Photochemical box model calculations were performed using measured concentrations, except for NO<sub>x</sub> and SO<sub>2</sub> which were varied over a wide range to simulate the plumes time evolution. Calculations show that OH concentrations and O<sub>3</sub> production efficiencies are qualitatively reasonable, given that dilution causes the plume to spend much of its lifetime with NO<sub>x</sub> concentrations below ~5 ppbv.

## Acknowledgements

The authors are indebted to the pilots and flight crew of the DOE G-1 for safe operations. Special acknowledgement is due chief pilot Bob Hannigan, whose navigational skills and positional awareness enabled accurate tracing of this plume. This paper has been authored with support from the Office of Biological and Environmental Research under Contract number DE-AC02-98CH10866. The US Government retains non-exclusive, royalty free license to publish or reproduce the published form of this contribution or to allow others to do so, for US Government purposes.

## References

Brock, C.A., et al., 2002. Particle growth in the plumes of coal-fired power plants. *Journal of Geophysics Research* 107 (D12), 4155.  
 Brock, C.A., et al., 2003. Particle growth in urban and industrial plumes in Texas. *Journal of Geophysics Research* 108 (D3), 4111.

EPA, National Emission Inventory (NEI) Database 1999 emission values accessible from [www.epa.gov/air/data/](http://www.epa.gov/air/data/), 2004.  
 Gillani, N.V., Meagher, J.F., Valente, R.J., Imhoff, R.E., Tanner, R.L., Luria, M., 1998. Relative production of ozone and nitrates in urban and rural power plant plumes 1. Composite results based on data from 10 field measurement days. *Journal of Geophysics Research* 103, 22,593–22,615.  
 Hewitt, C.N., 2001. The atmospheric chemistry of sulphur and nitrogen in power plant plumes. *Atmospheric Environment* 35, 1155–1170.  
 Jaenicke, R., Hanusch, T., 1993. Simulation of the optical particle counter forward scattering spectrometer probe 100 (FSSP-100), consequences for size distribution measurements. *Aerosol Science and Technology* 18, 309–322.  
 Karamchandani, P., Seigneur, C. Simulations of sulfate and nitrate chemistry in power plant plumes. *Journal of Air and Waste Management Association* 49, PM175–181.  
 Kleinman, L.I., Daum, P.H., Lee, Y.-N., Nunnermacker, L.J., Springston, S.R., Weinstein-Lloyd, J., Rudolph, J., 2002. Ozone production efficiency in an urban area. *Journal of Geophysics Research* 107 (D23), 4733.  
 Leaitch, W.R., Isaac, G.A., 1991. Tropospheric aerosol size distributions from 1982 to 1988 over Eastern North America. *Atmospheric Environment* 25a, 601–619.  
 Lee, Y.-N., Weber, R., Ma, Y., Orsini, D., Maxwell, K., Blake, D., Meinardi, S., Sachse, G., Harward, C., Chen, T.-Y., Thornton, D.C., Tu, F.H., Bandy, A.R., 2003. Airborne measurement of inorganic ionic components of fine aerosol particles using the PILS-IC technique during ACE-ASIA and TRACE-P. *Journal of Geophysics Research* 108, 8646.  
 Liu, Y., Daum, P.H., 2000. The effect of refractive index on size distributions and light scattering coefficients derived from optical particle counters. *Journal of Aerosol Science* 8, 945–957.  
 Luria, M., Tanner, R.L., Imhoff, R.E., Valente, R.J., Bailey, E.M., Mueller, S.F., 2000. Influence of natural hydrocarbons on ozone formation in an isolated power plant plume. *Journal of Geophysics Research* 105, 9177–9188.  
 Malm, W.C., Schichtel, B.A., Pitchford, M.L., Ashbaugh, L.L., Eldred, R.A., 2004. Spatial and monthly trends in speciated fine particle concentration in the United States. *Journal of Geophysics Research* 109, D03306.  
 McMurtry, P.H., Rader, D.J., Stith, J.L., 1981. Studies of aerosol formation in power plant plumes—I Growth laws for secondary aerosols in power plant plumes: implications for chemical conversion mechanisms. *Atmospheric Environment* 15, 2315–2327.  
 Moore II, K.G., et al., 2004. A comparison of similar aerosol measurements made on the NASA P3-B, DC-8, and NSF C-130 aircraft during TRACE-P and ACE-Asia. *Journal of Geophysics Research* 109, D15S15.  
 Nunnermacker, L.J., Imre, D., Daum, P.H., Kleinman, L., Lee, Y.-N., Lee, J.H., Springston, S.R., Newman, L., Weinstein-Lloyd, J., Luke, W.T., Banta, R., Alvarez, R., Senff, C., Sillman, S., Holdren, M., Keigley, G.W., Zhou, X., 1998. Characterization of the Nashville urban plume on July 3 and July 18, 1995. *Journal of Geophysics Research* 103, 28,129–28,148.  
 Nunnermacker, L.J., Kleinman, L.I., Imre, D., Daum, P.H., Lee, Y.-N., Lee, J.H., Springston, S.R., Newman, L.,

- Gillani, N., 2000.  $\text{NO}_y$  lifetimes and  $\text{O}_3$  production efficiencies in urban and power plant plumes: analysis of field data. *Journal of Geophysics Research* 105, 9165–9176.
- Ryerson, T.B., Buhr, M.P., Frost, G.J., Goldan, P.D., Holloway, J.S., Hübler, G., Jobson, B.T., Kuster, W.C., McKeen, S.A., Parrish, D.D., Roberts, J.M., Sueper, D.T., Trainer, M., Williams, J., Fehsenfeld, F.C., 1998. Emissions lifetimes and ozone formation in power plant plumes. *Journal of Geophysics Research* 103, 22,569–22,583.
- Ryerson, T.B., Trainer, M., Holloway, J.S., Parrish, D.D., Huey, L.G., Sueper, D.T., Frost, G.J., Donnelly, S.G., Schauffler, S., Atlas, E.L., Kuster, W.C., Goldan, P.D., Hübler, G., Meagher, J.F., Fehsenfeld, F.C., 2001. Observations of ozone formation in power plant plumes and implications for ozone control strategies. *Science* 292, 719–723.
- Sander, S.P., Golden, D.M., Kurylo, M.J., Huie, R.E., Orkin, V.L., Moortgat, G.K., Ravishankara, A.R., Kolb, C.E., Molina, M.J., Finalyson-Pitts, B.J., 2003. Chemical Kinetics and Photochemical Data for Use in Atmospheric Studies, Evaluation Number 14, JPL Publication 02-25. Jet Propulsion Laboratory, Pasadena.
- Stockwell, W.R., 1994. The effect of gas-phase chemistry on aqueous-phase sulfur dioxide oxidation rates. *Journal of Atmospheric Chemistry* 19, 317–329.
- Trainer, M., et al., 1993. Correlation of ozone with  $\text{NO}_y$  in photochemically aged air. *Journal of Geophysics Research* 98, 2917–2925.